Nanoscale Horizons

ROYAL SOCIETY OF CHEMISTRY

COMMUNICATION

View Article Online
View Journal

Cite this: DOI: 10.1039/d5nh00624d

Received 5th September 2025,
Accepted 10th February 2026

DOI: 10.1039/d5nh00624d

rsc.li/nanoscale-horizons

Similarity modulation mechanism in triboelectric nanogenerators

Bochao Xie, * Yingying Ma and Yihuang Xie

The central open question in triboelectric nanogenerators is not how much power they can deliver, but what dynamic principle governs the conversion from motion to charge. We answer this by establishing a similarity modulation mechanism that extends the classical *V*–*Q*–*x* relation into a predictive dynamic law. A single similarity descriptor $S_m = \omega_0 T$ organizes the electromechanical response across device geometries and operating modes under a clearly stated condition where dielectric relaxation and charge decay are slow relative to motion. Within this conditional similarity, normalized outputs collapse onto universal curves that reveal three regimes with simple design rules: a low frequency growth region, a resonance near $S_m \approx 2\pi$ that captures impedance alignment, and a high S_m ceiling where average power becomes frequency independent due to incomplete charge refresh per cycle. The framework also ranks input waveforms and shows why compact top hat profiles outperform sinusoids at fixed amplitude, and it provides explicit guidance for load matching and storage-oriented operation without introducing new empirical parameters. This theory converts scattered models into a single map that explains published trends, exposes real limits, and supplies a compact rule set for rational TENG design and scalable energy management.

New concepts

We demonstrate a similarity modulation mechanism (SMM) showing that triboelectric nanogenerators can be governed by one universal dynamic similarity control factor that compares how fast the device is mechanically driven with how fast charges and polarization can relax. Using this concept, we identify clear operating regimes that are easy to understand and apply: a regime where increasing driving speed boosts output, an optimum regime where energy transfer is most efficient, and a saturation regime where further speeding up no longer increases average power because interfacial charge cannot fully refresh within each cycle. This work adds new insight to nanoscience and nanotechnology by exposing the fundamental dynamic limit of contact electrification systems and enabling rational engineering of excitation waveforms, load matching, and power management strategies for scalable triboelectric energy harvesting and sensing.

1. Introduction

Triboelectric nanogenerators (TENGs)[1] have redefined the landscape of mechanical-to-electrical energy conversion. Unlike conventional electromagnetic systems, TENGs harness the coupling between contact electrification and electrostatic induction, a mechanism that endows them with extraordinary design flexibility, scalability, and environmental adaptability. Over the past decade, this paradigm has inspired advances across multiple fronts—ranging from material design and microfabrication,[2,3] energy management and circuit engineering,[4,5] and the physics of charge generation,[6,7] to application-driven device innovations.[8–10] Yet, beneath this rapid technological progress, a crucial aspect remains fundamentally incomplete: the understanding of TENG dynamics, the very mechanism dictating how mechanical motion is translated into electrical output.

The dynamic behavior of TENGs defines the bridge between mechanical excitation and electrical response, determining not only the instantaneous performance but also the scaling limits and design logic of the entire technology. In principle, this dynamic coupling is encapsulated by the governing *V*–*Q*–*x* relationship, which links voltage (V), transferred charge (Q), and displacement (x) through a capacitor-like framework.[11] Originating from the contact-separation model, this relationship has been extended to other operation modes[12] and to structured systems such as grating-based generators.[13,14] Later works constructed first-principles derivations from electrostatic or Maxwell formulations,[15–22] reaffirming that triboelectric conversion is not an empirical phenomenon, but a self-consistent electromechanical process.

However, the *V*–*Q*–*x* formalism, despite its elegance, captures only the static or quasi-steady coupling among these variables. It does not yet provide a unified dynamic theory capable of describing how external excitations, structural parameters, and circuit conditions collectively shape system

School of Engineering & Applied Science, Yale University, New Haven 06250, USA. E-mail: bochao.xie@yale.edu

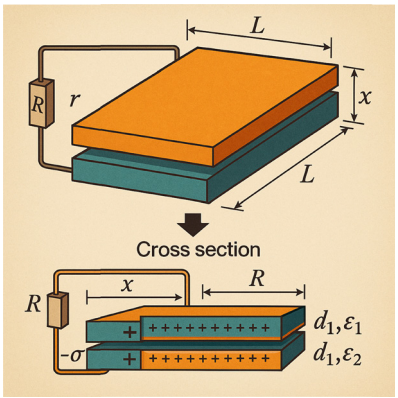

Fig. 1 Schematic of the structures of the TENG.

evolution. As a result, existing models often treat motion input, device structure, and load impedance as independent variables—an assumption that oversimplifies the inherently coupled nature of TENG operation.[23–30] The absence of such a dynamic unification has constrained the field to empirical optimization rather than predictive design.

In this work, we address this missing foundation by introducing a similar theory based analytical framework that reformulates TENG dynamics into a dimensionless, self-scaling representation. This framework reveals that the entire electromechanical behavior of a TENG can be governed by a single similarity descriptor that couples the mechanical timescale of motion and the electrical relaxation of the circuit. Within this formalism, diverse structural modes and excitation forms collapse into a unified dynamic landscape, allowing direct interpretation of power scaling, motion regimes, and saturation behavior from a common theoretical perspective (Fig. 1).

2. Results

2.1. A universal scaling law for triboelectric nanogenerators

The electro-mechanical coupling in triboelectric nanogenerators (TENGs) can be fundamentally described by the dynamic equation:

$$R\frac{\mathrm{d}Q}{\mathrm{d}t} = V_{\mathrm{OC}}(x) - \frac{Q}{C(x)} = \frac{Q_{\mathrm{SC}}(x)}{C(x)} - \frac{Q}{C(x)}$$

where the system variables include the transferred charge Q, load resistance R, position-dependent capacitance $C(x)$, open circuit voltage $V_{\mathrm{OC}}(x)$, and short-circuit transferred charge $Q_{\mathrm{SC}}(x)$. The emergence of a universal scaling parameter becomes apparent through non-dimensional analysis. Introducing the dimensionless variables $\hat{t} = t/T$, $\hat{Q} = Q/q$, and $\hat{C} = C/C_0$, where T represents the characteristic time scale, q denotes the characteristic charge, and C_0 signifies the characteristic capacitance, we obtain the normalized governing equation:

$$\frac{1}{S_{\mathrm{m}}}\frac{\mathrm{d}\hat{Q}}{\mathrm{d}\hat{t}} + \hat{g}\hat{Q} = \hat{g}\hat{j}$$

Here, the dimensionless functions are defined as $\hat{g}^{-1} = C/C_0$ and $\hat{j} = Q_{\mathrm{SC}}/q$, while the crucial similarity parameter emerges as $S_{\mathrm{m}} = \omega_0 T = T/(RC_0)$. The theoretical framework reveals that S_{m} serves as the fundamental similarity criterion governing TENG dynamics. While the structural functions $\hat{g} = \hat{g}(\hat{x})$ and $\hat{j} = \hat{j}(\hat{x})$ depend exclusively on dimensionless displacement $\hat{x} = x/D$ and define the specific geometric characteristics of each TENG configuration, S_{m} remains independent of displacement or time variables. This leads to our central conclusion: two structurally analogous TENGs experiencing kinematically similar motion will demonstrate completely scalable performance, provided they share identical S_{m} values. The physical significance of $\omega_0 = 1/(RC_0)$ corresponds to the characteristic frequency of the equivalent RC circuit formed by the initial TENG capacitance and external load, thereby providing concrete physical meaning to the similarity parameter. The general solution formalism for the system dynamics can be expressed as:

$$\hat{Q}(\hat{t}) = \frac{1}{\hat{K}}\int \hat{j}\,\mathrm{d}\hat{K},$$

where

$$\hat{K} = \exp\left(S_{\mathrm{m}}\hat{G}\right) = \exp\left(S_{\mathrm{m}}\int \hat{g}\,\mathrm{d}\hat{t}\right)$$

with the corresponding current output given by:

$$I = \omega_0 q\hat{g}(\hat{j} - \hat{Q})$$

This theoretical construct provides a comprehensive framework where analysing any specific TENG design simply requires incorporating its structural relations $\hat{g}(\hat{x})$ and $\hat{j}(\hat{x})$. For a lateral-sliding mode TENG, the structural characteristic relations adopt particularly elegant forms. The capacitance follows $C = \varepsilon_0 W(L - x)/\delta$, while the short-circuit charge increases linearly as $Q_{\mathrm{SC}} = \sigma x W$. Here, the effective thickness is defined as $\delta = \varepsilon_0 d_1/\varepsilon_1 + \varepsilon_0 d_2/\varepsilon_2$. The corresponding dimensionless variables become $\hat{x} = x/L$, $\hat{g} = (1 - \hat{x})^{-1}$, and $\hat{j} = \hat{x}$, with the characteristic frequency given by $\omega_0 = \delta/(\varepsilon_0 WLR)$. This similarity framework underscores a fundamental distinction between TENGs and electromagnetic generators. While EMGs with analogous structures exhibit unconditional similarity due to the absence of governing dimensionless groups in their dynamic equations (as detailed in the SI), the existence of the S_{m} criterion in TENGs fundamentally explains their rich and complex dynamic behaviours. The presence of this scaling parameter enables both precise performance prediction and systematic device optimization across diverse configurations and operating conditions.

2.2. The emergence of periodicity in TENG dynamics

While electromagnetic generators inherently exhibit periodic outputs under cyclic excitation, the periodicity of triboelectric nanogenerator (TENG) solutions is a non-trivial consequence of system dynamics. For a periodic mechanical input $x(t)$ with period T, the corresponding dimensionless displacement $\hat{x}(\hat{t})$ possesses a unit period. The general solution for the dimensionless transferred charge can be expressed as:

$$\hat{Q}(\hat{t}) = \hat{Q}(1)\frac{1 - \hat{K}^{-N}(1)}{1 - \hat{K}^{-1}(1)}\frac{1}{\hat{K}\left(\hat{\xi}\right)} + \hat{Q}\left(\hat{\xi}\right)$$

where $\hat{\xi} = \hat{t} - N \in [0,1)$ and N is a non-negative integer. This representation demonstrates that the charge dynamics over the semi-infinite time domain $\hat{t} \in [0,+\infty)$ are completely determined by their behavior within a single, finite period $\hat{t} \in [0,1]$.

As time evolves ($\hat{t} \to +\infty$), the ratio of successive periods satisfies $\hat{Q}(\hat{t}+1)/\hat{Q}(\hat{t}) \to 1$, confirming the asymptotic convergence to a steady-state periodic solution $\hat{Q}^{S}(\hat{t})$. This periodic limit cycle can be compactly defined for $\hat{t} \in [0,1)$ as:

$$\hat{Q}^{S}(\hat{t}) = \frac{\hat{Q}(1)}{1-\hat{K}^{-1}(1)}\frac{1}{\hat{K}(\hat{t})} + \hat{Q}(\hat{t})$$

This establishes that despite the complex, state-dependent capacitance, TENGs under periodic excitation inevitably converge to a unique periodic operating regime.

2.3. Fundamental limits and scaling behavior

2.3.1. The high-frequency limit ($S_m \to 0$). In the regime where the motion period is much shorter than the electrical relaxation time ($S_m = T/(RC_0) \to 0$), the governing equation simplifies to $d\hat{Q}^{S}_{S_m\to 0}\Big/d\hat{t} = 0$, indicating that the dimensionless transferred charge approaches a constant value:

$$\hat{Q}^{S}_{S_m\to 0} = 1 - \frac{1}{\int_0^1 \hat{g}\,d\hat{t}} = 1 - \frac{1}{\hat{G}(1)}$$

Physically, this limit represents insufficient time for charge redistribution during rapid oscillations, causing the transferred charge to saturate. Consequently, the current and voltage become:

$$I^{S}_{S_m\to 0} = \frac{\sigma\delta}{\varepsilon_0 R}\left(\frac{\hat{g}}{\hat{G}(1)} - 1\right), \quad V^{S}_{S_m\to 0} = \frac{\sigma\delta}{\varepsilon_0}\left(\frac{\hat{g}}{\hat{G}(1)} - 1\right)$$

Remarkably, in this limit, the output current becomes independent of both the excitation frequency T^{-1} and the device's primary dimensions L and W, imposing a fundamental upper bound on power generation. This saturation behavior, absent in EMGs, reveals a unique scaling law for TENGs. Furthermore, the output voltage becomes load-independent, characterizing the TENG as an ideal voltage source in this operational regime.

2.3.2. The low-frequency limit ($S_m \to \infty$). Conversely, when motion is sufficiently slow ($S_m \to \infty$), the system approaches quasi-static equilibrium, yielding:

$$\hat{Q}^{S}_{S_m\to\infty} = \hat{j} = \hat{x}$$

This indicates complete charge transfer tracking the short-circuit value Q_{SC}. The resulting current and voltage scale as:

$$I^{S}_{S_m\to\infty} = \frac{\sigma WL}{T}\frac{d\hat{x}}{d\hat{t}}, \quad V^{S}_{S_m\to\infty} = \frac{\sigma WLR}{T}\frac{d\hat{x}}{d\hat{t}}$$

In this regime, both current and voltage exhibit conventional $1/T$ scaling, similar to EMGs. However, a fundamental distinction remains: the TENG operates as a current source, whereas the EMG behaves as a voltage source, reflecting their different energy conversion mechanisms.

The contrasting limiting behaviours produce a distinctive scaling law for the average output power $\bar{P}^{S}$. For EMGs, power universally scales as $\bar{P} \propto T^{-2}$. For TENGs, the scaling is regime-dependent:

As $T \to 0$ ($S_m \to 0$):

$$\bar{P}^{S}_{T\to 0} = \frac{\sigma^2\delta^2}{\varepsilon_0^2 R}\int_0^1 \left(\frac{\hat{g}}{\hat{G}(1)} - 1\right)^2 d\hat{t}$$

The power saturates to a finite constant, independent of both frequency and device dimensions.

As $T \to \infty$ ($S_m \to \infty$):

$$\bar{P}^{S}_{T\to\infty} = \frac{\sigma^2 W^2 L^2 R}{T^2}\int_0^1 \left(\frac{d\hat{x}}{d\hat{t}}\right)^2 d\hat{t}$$

The power recovers the conventional T^{-2} scaling.

At finite periods, the average power $\bar{P}^{S} = T^{-1}\int_0^T (I^{S})^2 R\,d\hat{t}$ smoothly transitions between these asymptotic limits, creating a universal scaling curve that encapsulates the fundamental performance limits of TENGs across all operating conditions.

2.4. Optimal motion input

Our analysis reveals an upper power saturation limit as $T \to 0$, which is independent of frequency and primary scales but critically dependent on the dimensionless motion input $\hat{x}(\hat{t})$. This finding prompts a fundamental question: what form of $\hat{x}(\hat{t})$—hereafter termed the shape function—maximizes the average output power ($\bar{P}^{S}_{T\to 0}$) under this limiting condition?

The theoretical optimum is a top-hat function, given by:

$$\hat{x}_{opt}(\hat{t}) = \begin{cases} \hat{x}_m, & 0 \le \hat{t} \le \dfrac{1}{\hat{g}_m + 1} \\ 0, & \dfrac{1}{\hat{g}_m + 1} < \hat{t} \le 1 \end{cases}$$

where $\hat{g}_m = \hat{g}(\hat{x}_m)$. This waveform yields the maximum achievable power,

$$\max\left(\left(\bar{P}^{S}_{T\to 0}\right)\right) = \frac{1}{4}\omega_0^2 q^2 R\frac{(\hat{g}_m - 1)^2}{\hat{g}_m},$$

and a synchronous, piecewise-constant current output,

$$I^{S}_{T\to 0} = \begin{cases} \dfrac{1}{2}\omega_0 q(\hat{g}_m - 1), & 0 \le \hat{t} \le \dfrac{1}{\hat{g}_m + 1} \\ \dfrac{1}{2}\omega_0 q\left(\dfrac{1}{\hat{g}_m} - 1\right), & \dfrac{1}{\hat{g}_m + 1} < \hat{t} \le 1 \end{cases}$$

The optimal shape function for T is a top-hat form, fully determined by the structural characteristic $\hat{g}(\hat{x})$ and the displacement limit $\hat{x}_m$. The resulting current waveform is synchronous with the motion input, suggesting the potential for a mechanical power management strategy.

We further employed numerical simulations to evaluate the performance of $\hat{x}_{opt}$ at finite periods, comparing it against harmonic ($\hat{x}^{Har}$), triangular ($\hat{x}^{Tri}$), and two composite waveforms ($\hat{x}^{Har}_{opt}$, $\hat{x}^{Tri}_{opt}$; see the SI). The corresponding $\bar{P}^{S}$–T curves are shown in Fig. 2. Evidently, the power output for $\hat{x}_{opt}$ markedly surpasses that of other inputs. Furthermore, the composite waveforms $\hat{x}^{Har}_{opt}$ and $\hat{x}^{Tri}_{opt}$ outperform their pure counterparts,

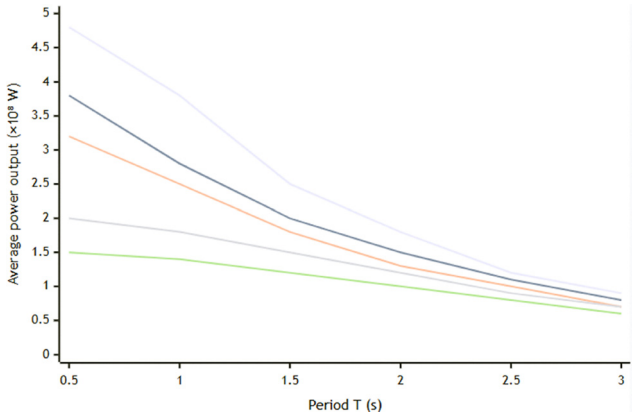

Fig. 2 Comparison of $\bar{P}^S$–T curves corresponding to different shape functions.

indicating that intermittent and abrupt motion profiles enhance the average power output under identical motion periods.

It should be noted that the optimal function $\hat{x}_{opt}$ is derived under the condition where period T approaches zero, and its advantages are maintained under relatively high frequency conditions.

2.5. Motion input decomposition and intermittent operation

The performance advantage of composite waveforms $\hat{x}_{opt}^{Har}$ and $\hat{x}_{opt}^{Tri}$ over pure harmonic and triangular waves at high frequencies requires careful analysis. Since these composite waveforms feature steeper transitions, we develop the concept of motion input decomposition to compare waveforms with identical maximum velocities.

As shown in Fig. 3, we analyze a sequence of motions where motion 1 (a single continuous cycle) is progressively decomposed into multiple intermittent sub-cycles: motion 2 (two sub-cycles), motion 3 (three sub-cycles), motion 4 (four sub-cycles), motion 5 (six sub-cycles), and motion 6 (twelve sub-cycles). The mathematical form of these decomposed motions is given by:

$$\hat{x}_i(\hat{t}) = \frac{\hat{x}_m}{2}[1 - \cos(2\pi f_i(\hat{t}))] \cdot \Pi_i(\hat{t})$$

where $f_i(\hat{t}) = N_i\hat{t}$ for $0 \le \hat{t} \le N_i^{-1}$, and $\Pi_i(\hat{t})$ represents a rectangular window function that is unity within each active sub-interval and zero elsewhere. The decomposition levels correspond to $N_i = \{1, 2, 3, 4, 6, 12\}$ for i = 1–6, respectively.

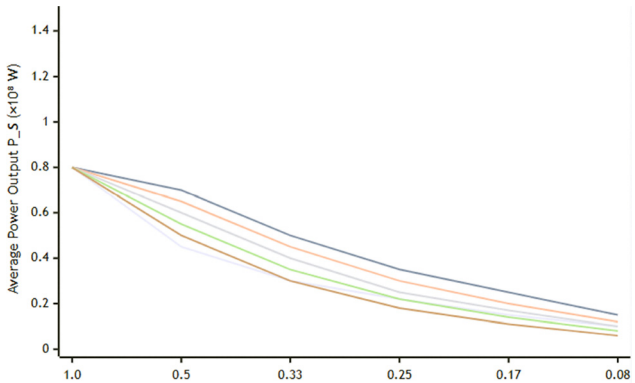

Fig. 3 Motion input decomposition and corresponding $\bar{P}^S$–T_{eff} curves.

To ensure kinematic consistency, we define the effective period $T_{eff} = T{\cdot}N_i^{-1}$, representing the duration of each active motion segment. This normalization guarantees identical maximum velocities when comparing different waveforms at the same T_{eff}. The power output analysis reveals a distinct optimum in the decomposition strategy. Motion 2 demonstrates enhanced power generation at shorter effective periods compared to the continuous motion 1. However, this trend reverses with excessive decomposition – motions 3 through 6 exhibit progressively reduced performance across all frequencies. This establishes motion 2 as the optimal decomposition level, whose waveform characteristics most closely resemble the beneficial properties of $\hat{x}_{opt}^{Har}$, confirming that moderate intermittency rather than maximal decomposition maximizes power output.

2.6. Optimal load impedance and resonant energy transfer in TENG systems

The power delivery characteristics of triboelectric nanogenerators reveal a fundamental distinction from conventional electromagnetic generators. While electromagnetic systems typically exhibit negligible optimal load resistance, TENGs demonstrate a well-defined maximum power point at a characteristic impedance R_{opt} that depends critically on both structural and operational parameters. This section establishes the underlying principle governing this optimal impedance condition and its relationship to resonant energy transfer.

For a specified motion profile, theoretical analysis confirms the existence of a unique dimensionless parameter S_m^* that maximizes power extraction. The corresponding optimal load resistance follows the scaling law:

$$R_{opt} = \frac{\delta}{\varepsilon_0 WL} \cdot \frac{T}{S_m^*}$$

Experimental validation across four distinct operational regimes—varying in device dimensions and excitation period—confirms this relationship. The power-resistance characteristics consistently peak at $S_m^* \approx 2.810$ despite parametric variations, demonstrating the universal criterion for impedance matching in TENG systems.

For harmonic excitation profiles, the optimal similarity parameter admits a closed-form expression:

$$S_m^* = 2\pi(1 - \hat{x}_m)^{1/2}$$

The characteristically large magnitude of R_{opt} emerges naturally from this scaling relationship, accounting for the fundamental constant and typical displacement ranges in practical systems.

Further analysis reveals a profound physical interpretation: maximum power transfer occurs when the mechanical excitation frequency synchronizes with the system's electrical response. This resonant condition satisfies:

$$\frac{2\pi}{T} = \frac{1}{T}\int_0^T \frac{dt}{R_{opt}C(t)} = \langle \omega_{RC} \rangle$$

where the right-hand side represents the period-averaged

natural frequency of the time-varying RC network. This resonance condition establishes a universal design principle for optimal energy harvesting.

The general expression for optimal load resistance under resonant operation becomes:

$$R_{\mathrm{opt}} = \frac{T}{2\pi\varepsilon_0 WL} \cdot \frac{\delta}{\langle \hat{g} \rangle}$$

where $\langle \hat{g} \rangle = \int_0^1 \hat{g} \mathrm{d}\hat{t}$. Experimental validation using published data confirms the predictive capability of this formulation, with the model achieving agreement within one order of magnitude across diverse experimental configurations. This resonant impedance matching framework provides a physical basis for TENG optimization, advancing beyond empirical approaches toward principled design methodologies.

3. Conclusion

This work establishes that the complex dynamics arising from the governing equation endow TENGs with fundamentally different characteristics from EMGs, characteristics that are significantly richer, more complex, and often counter-intuitive. These findings provide crucial insights for the structural design and application positioning of TENGs.

The operation of EMGs is unconditionally similar, whereas the similarity of TENGs depends exclusively on the similarity number $S_{\mathrm{m}} = \omega_0 T$, where ω_0 represents the characteristic frequency of the TENG structure and T is the motion input period. The operating states of TENG systems can be categorized based on the value of S_{m} into high-frequency ($S_{\mathrm{m}} \ll 2\pi$), medium-frequency ($S_{\mathrm{m}} \sim 2\pi$), and low-frequency ($S_{\mathrm{m}} \gg 2\pi$) states, each exhibiting distinct dynamic characteristics.

The output of an EMG depends solely on the instantaneous motion input, while the output of a TENG exhibits history-dependent behaviour. Under periodic motion excitation, the EMG output is inherently periodic, whereas the TENG output asymptotically approaches a periodic solution. In terms of power source characteristics, the EMG behaves as a voltage source, while the TENG exhibits voltage-source characteristics in the high-frequency state and transitions to current-source behaviour in the low-frequency state.

The energy output scaling reveals another fundamental difference: the average output power of an EMG follows an inverse-square relationship with the input period ($\bar{P} \propto T^{-2}$), while the TENG maintains this relationship only in the low-frequency state but saturates to a frequency-independent constant in the high-frequency state. Furthermore, in the high-frequency state, the TENG exhibits an optimal motion input in the form of a top-hat function, whose specific form is determined solely by displacement constraints and structural characteristics. The power output can be enhanced through appropriate motion decomposition and intermittent operation strategies, and a resonance state exists where the matching resistance corresponds to the condition where the time-averaged oscillation frequency equals the input motion frequency.

The distinctive dynamics of TENGs suggests that their design and application demand innovative approaches fundamentally different from those used for EMGs. The significantly greater complexity of TENG dynamics, particularly the strong coupling among motion input parameters, structural parameters, and load circuit parameters, indicates that advancing TENG technology requires collaborative efforts and deep integration across multiple disciplines, including materials science, structural design, power management, and dynamic analysis. These findings not only provide a theoretical foundation for TENG optimization but also open new research directions for overcoming fundamental limitations in mechanical energy harvesting systems.

4. Methods

4.1. Theoretical framework development

The dynamic analysis framework for TENG systems was established through systematic derivation from fundamental electromechanical principles. Beginning with the intrinsic relationship among transferred charge, voltage, and displacement, we applied the Buckingham π theorem to identify the key dimensionless groups governing system behaviour. This approach yielded a universal theoretical framework capable of describing TENG operation across multiple scales and configurations.

4.2. Computational methodology

We developed a novel numerical algorithm specifically designed for efficient simulation of TENG dynamics under arbitrary motion profiles. The computational scheme employs a discrete recursive formulation:

The charge state evolves according to:

$$\hat{Q}[n] = \frac{\sum_{j=1}^{n} \hat{J}[j] \cdot \Delta\hat{K}[j]}{\hat{K}[n]}$$

where the integrating factors are computed as:

$$\hat{K}[n] = \exp\left(S_{\mathrm{m}} \cdot \sum_{j=1}^{n} \hat{g}[j] \cdot \Delta\hat{t} \right)$$

Initialization is defined by: $\hat{Q}[0] = 0$, $\hat{K}[0] = 1$.

For determining steady-state periodic solutions, we derived a direct computational approach:

$$\hat{Q}_{\mathrm{s}}[n] = \frac{\hat{Q}[N]}{1 - \hat{K}[N]^{-1}} \cdot \hat{K}[n]^{-1} + \hat{Q}[n]$$

where N represents the discretization of one complete period. This formulation provides numerical stability by circumventing potential overflow issues associated with the exponential terms in long-time simulations.

Conflicts of interest

There are no conflicts to declare.

Data availability

All data supporting the findings of this study, including analytical derivations, numerical simulation scripts, and supplementary figures, are available within the article and its supplementary information (SI). Supplementary information is available. See DOI: https://doi.org/10.1039/d5nh00624d.

Additional data related to numerical codes and model validation can be provided by the corresponding author upon reasonable request.

References

1 F. Fan, Z. Tian and Z. L. Wang, Flexible triboelectric generator!, *Nano Energy*, 2012, **1**(2), 328–334.
2 H. Zou, Y. Zhang, L. Guo, P. Wang, X. He and G. Dai, *et al.*, Quantifying the triboelectric series, *Nat. Commun.*, 2019, **10**, 1427.
3 W. Wang, A. Yu, X. Liu, Y. Liu, Y. Zhang and Y. Zhu, *et al.*, Large-scale fabrication of robust textile triboelectric nanogenerators, *Nano Energy*, 2020, **71**, 104605.
4 H. Zhang, Y. Chen, L. Deng, X. Zhu, C. Xu and L. Xie, *et al.*, Efficient electrical energy conversion strategies from triboelectric nanogenerators to practical applications: A review, *Nano Energy*, 2024, **132**, 110383.
5 C. Qi, Z. Yang, J. Zhi, R. Zhang, J. Wen and Y. Qin, Enhancing the powering ability of triboelectric nanogenerator through output signal's management strategies, *Nano Res.*, 2023, **16**(9, SI), 11783–11800.
6 L. Zhou, D. Liu, J. Wang and Z. L. Wang, Triboelectric nanogenerators: Fundamental physics and potential applications, *Friction*, 2020, **8**(3), 481–506.
7 Y. Li, Y. Luo, S. Xiao, C. Zhang, C. Pan and F. Zeng, *et al.*, Visualization and standardized quantification of surface charge density for triboelectric materials, *Nat. Commun.*, 2024, **15**, 6004.
8 A. Li, Z. Qiliang, Y. Mi, H. U. Rehman, M. Shoaib and X. Cao, *et al.*, Triboelectric nanogenerator drives electrochemical water splitting for hydrogen production: Fundamentals, progress, and challenges, *Small*, 2025, **21**, 2407043.
9 J. He, X. Wang, Y. Nan and H. Zhou, Research progress of triboelectric nanogenerators for ocean wave energy harvesting, *Small*, 2025, **21**, 2411074.
10 G. Khandelwal, N. P. M. J. Raj and S. J. Kim, Triboelectric nanogenerator for healthcare and biomedical applications, *Nano Today*, 2020, **33**, 100882.
11 S. Niu, S. Wang, L. Lin, Y. Liu, Y. S. Zhou and Y. Hu, *et al.*, Theoretical study of contact-mode triboelectric nanogenerators as an effective power source, *Energy Environ. Sci.*, 2013, **6**(12), 3576–3583.
12 S. Niu and Z. L. Wang, Theoretical systems of triboelectric nanogenerators, *Nano Energy*, 2015, **14**(SI), 161–192.
13 G. Zhu, J. Chen, Y. Liu, P. Bai, Y. S. Zhou and Q. Jing, *et al.*, Linear-grating triboelectric generator based on sliding electrification, *Nano Lett.*, 2013, **13**(5), 2282–2289.
14 S. Niu, S. Wang, Y. Liu, Y. S. Zhou, L. Lin and Y. Hu, *et al.*, A theoretical study of grating structured triboelectric nanogenerators, *Energy Environ. Sci.*, 2014, **7**(7), 2339–2349.
15 J. Shao, M. Willatzen, Y. Shi and Z. L. Wang, 3d mathematical model of contact-separation and single-electrode mode triboelectric nanogenerators, *Nano Energy*, 2019, **60**, 630–640.
16 X. Li, T. H. Lau, D. Guan and Y. Zi, A universal method for quantitative analysis of triboelectric nanogenerators, *J. Mater. Chem. A*, 2019, **7**(33), 19485–19494.
17 H. Zhao, H. Wang, H. Yu, Q. Xu, X. Li and J. Guo, *et al.*, Theoretical modeling of contact-separation mode triboelectric nanogenerators from initial charge distribution, *Energy Environ. Sci.*, 2024, **17**(6), 2228–2247.
18 X. Guo, J. Shao, M. Willatzen, Y. Yang and Z. L. Wang, Theoretical model and optimal output of a cylindrical triboelectric nanogenerator, *Nano Energy*, 2022, **92**, 106762.
19 J. Shao, M. Willatzen and Z. L. Wang, Theoretical modeling of triboelectric nanogenerators (tengs), *J. Appl. Phys.*, 2020, **128**, 111101.
20 Z. L. Wang, On the first principle theory of nanogenerators from Maxwell's equations, *Nano Energy*, 2020, **68**, 104272.
21 R. L. Bulathsinghala, J. H. B. Deane and R. D. I. G. Dharmasena, The distance-dependent electric field theory for sliding mode triboelectric nanogenerators, *Adv. Energy Mater.*, 2025, **15**, 2403853.
22 R. D. I. G. Dharmasena, K. D. G. I. Jayawardena, C. A. Mills, R. A. Dorey and S. R. P. Silva, A unified theoretical model for triboelectric nanogenerators, *Nano Energy*, 2018, **48**, 391–400.
23 S. Zargari, A. Rezania, Z. D. Koozehkanani, H. Veladi, J. Sobhi and L. Rosendahl, Effect of the inherent capacitance optimization on the output performance of triboelectric nanogenerators, *Nano Energy*, 2022, **92**, 106740.
24 S. Niu, Y. Liu, Y. S. Zhou, S. Wang, L. Lin and Z. L. Wang, Optimization of triboelectric nanogenerator charging systems for efficient energy harvesting and storage, *IEEE Trans. Electron Devices*, 2015, **62**(2), 641–647.
25 W. Liu and J. Shi, A dynamics model of triboelectric nanogenerator transducers, *Nano Energy*, 2021, **89**, 106479.
26 Y. Zi, S. Niu, J. Wang, Z. Wen, W. Tang and Z. L. Wang, Standards and figure-of-merits for quantifying the performance of triboelectric nanogenerators, *Nat. Commun.*, 2015, **6**, 8376.
27 D. Zhao, X. Yu, J. Wang, Q. Gao, Z. Wang and T. Cheng, *et al.*, A standard for normalizing the outputs of triboelectric nanogenerators in various modes, *Energy Environ. Sci.*, 2022, **15**(9), 3901–3911.
28 R. D. I. G. Dharmasena, K. D. G. I. Jayawardena, C. A. Mills, J. H. B. Deane, J. V. Anguita and R. A. Dorey, *et al.*, Triboelectric nanogenerators: providing a fundamental framework, *Energy Environ. Sci.*, 2017, **10**(8), 1801–1811.
29 R. D. I. G. Dharmasena, J. H. B. Deane and S. R. P. Silva, Nature of power generation and output optimization criteria for triboelectric nanogenerators, *Adv. Energy Mater.*, 2018, **8**, 1802190.
30 B. Sun, X. Guo, Y. Zhang, Z. L. Wang and J. Shao, A generalized model for a triboelectric nanogenerator energy harvesting system, *Nano Energy*, 2024, **126**, 109637.

